European Journal of Pharmaceutics and Biopharmaceutics 191 (2023) 265–275

Contents lists available at ScienceDirect

European Journal of Pharmaceutics and Biopharmaceutics

journal homepage: www.elsevier.com/locate/ejpb

Research paper

Microstructural insight into inhalation powder blends through correlative multi-scale X-ray computed tomography

Parmesh Gajjar [a,b,c,d,*], Ioanna Danai Styliari [e], Victoria Legh-Land [e], Hrishikesh Bale [f], Benjamin Tordoff [g], Philip J. Withers [a,b,c], Darragh Murnane [e,*]

[a] Henry Moseley X-ray Imaging Facility, Department of Materials, The University of Manchester, Manchester M13 9PL, UK
[b] National Facility for Laboratory X-ray Computed Tomography, The University of Manchester, Manchester M13 9PL, UK
[c] Henry Royce Institute for Advanced Materials, Oxford Road, Manchester M13 9PL, UK
[d] Seda Pharmaceutical Development Services, Unit D, Oakfield Road, Cheadle Royal Business Park, Stockport SK8 3GX, UK
[e] School of Life and Medical Sciences, University of Hertfordshire, College Lane, Hatfield AL10 9AB, UK
[f] Carl Zeiss X-ray Microscopy, 5300 Central Parkway, Dublin, CA 94568, USA
[g] Carl Zeiss Microscopy GmbH, Carl-Zeiss-Straße 22, 73447 Oberkochen, Germany

ARTICLE INFO

Keywords:
X-ray computed tomography
Microstructural equivalence
Powder characterisation
Inhalation
Correlative tomography
Microstructure

ABSTRACT

Dry powder inhalers (DPI) are important for topical drug delivery to the lungs, but characterising the pre-aerosolised powder microstructure is a key initial step in understanding the post-aerosolised blend performance. In this work, we characterise the pre-aerosolised 3D microstructure of an inhalation blend using correlative multi-scale X-ray Computed Tomography (XCT), identifying lactose and drug-rich phases at multiple length scales on the same sample. The drug-rich phase distribution across the sample is shown to be homogeneous on a bulk scale but heterogeneous on a particulate scale, with individual clusters containing different amounts of drug-rich phase, and different parts of a carrier particle coated with different amounts of drug-rich phase. Simple scalings of the drug-rich phase thickness with carrier particle size are used to derive the drug-proportion to carrier particle size relationship. This work opens new doors to micro-structural assessment of inhalation powders that could be invaluable for bioequivalence assessment of dry powder inhalers.

1. Introduction

Although COVID-19 has brought respiratory illness to the forefront of public interest, for many people chronic respiratory diseases are a way of life. There are an estimated 339 million asthma suffers worldwide [1], with approximately 1000 worldwide deaths per day. Chronic Obstructive Pulmonary Disease (COPD) is estimated to become the third leading cause of death by 2030 while chronic lower respiratory disease (mainly COPD) is the third leading cause of death in the USA [2]. For long term patients of chronic respiratory diseases, daily inhaled medications are a way of life, and access to low-cost portable therapies is vital.

An important part of the development of lower cost generic products is demonstrating pharmaceutical equivalence and bioequivalence (BE) between the generic developmental and reference products [3]. BE is defined as the absence of significant difference in the rate and extent to which the active pharmaceutical ingredient(s) (API) reaches the site of drug action, when the same dose is administered under similar conditions [4]. For systemically acting drugs, BE is typically measured using pharmacokinetic (PK) studies, comparing the maximum plasma concentration (C_{max}), time taken to reach this maximum (t_{max}), and the total plasma concentration over time (AUC) between the test and reference products [5]. However, PK studies alone have limited use in BE assessment for locally acting drugs since the drug is delivered directly to the site of action [6–10] without the need for systemic circulation. For instance, topical formulations are applied directly to the skin and inhaled therapies are inhaled straight to the lungs. Instead of relying on PK studies alone, the US Food and Drug Administration (FDA) uses a weight of evidence approach, combining in-vitro, PK, pharmacodynamic (PD) and clinical studies to demonstrate BE for locally acting drug products. At the same time, alternative pathways to demonstrate BE are being explored.

The FDA introduced the idea of microstructural equivalence (Q3) to differentiate between formulations possessing different internal spatial

* Corresponding author.
E-mail addresses: parmesh.gajjar@alumni.manchester.ac.uk (P. Gajjar), d.murnane@herts.ac.uk (D. Murnane).

https://doi.org/10.1016/j.ejpb.2023.08.016
Received 17 April 2023; Received in revised form 9 August 2023; Accepted 25 August 2023
Available online 30 August 2023

arrangements of the same components (Q1) in the same concentrations (Q2). For topical formulations, Q3 microstructural assessment has allowed direct comparison between products which are Q1 and Q2 equivalent, and thus it is a vital tool in demonstrating BE [6]. Inhaled therapies have additional complexity since patient-device-formulation interactions to aerosolise the product have a significant influence on the microstructure of the aerosolized product, alongside manufacturing and formulation processes [11]. Price et al. [12,13] recently pioneered the use of morphology-direct Raman spectroscopy (MDRS) orthogonally alongside in-vitro dissolution testing to detect subtle differences in post-aerosolised dry powder inhaler product (DPIs). However, the link between the pre-aerosolisation and the post-aerosolisation microstructures critically remains unknown. Understanding the pre-aerosolised formulation microstructure and its influence on product performance is vital for the Q3 assessment of inhaled DPI formulations.

There are a wide variety of powder characterisation techniques to measure size, shape and chemical mapping, however many require aerosolising or disturbing the powder. For instance laser diffraction can measure the particle size distribution of powder, but requires full aerosolisation or dispersion in a liquid medium. Microscopy methods (electron or optical) are often used to assess shape, but these too require dispersion of the powder onto a slide. Recently, X-ray Computed Tomography (XCT, with a primer available in [14]) has emerged as a useful technique for examining powder-beds, allowing assessment of the powder bed density, particle size, particle shape and inter-crystal interactions without disturbing the powder arrangements [15–19]. The introduction of X-ray optical elements has increased the resolution of laboratory XCT systems, with these particular instruments known as "X-ray microscopes" due to their similarity with light microscopy methods [20–23]. Previously we have shown how micro-XCT on such instruments can be used to characterise α-lactose monohydrate, a common excipient in inhalation formulations [16]. Inhalation powder blends are more complex due to the addition of fine material in the size range 1 μm to 5 μm required for inhalation, which also have similar densities to the excipient lactose. This presents a strong challenge to both the resolution and contrast of laboratory micro-XCT systems.

A second challenge arises from the multiple length scales of interest for inhalation blends, with the fine material (e.g. API particles) typically having a size less than 5 μm but the carrier lactose lying in the size range 50 μm to 150 μm. Micro-scale XCT (micro-XCT) is well suited for powders of the size range greater than 50 μm [15,16], however the fine material is very close to the limit of resolution of this technique. On the other hand, nano-scale XCT (nano-XCT) can be used for characterising powders closer to 1 μm in size [24], but would be unsuitable for the larger particles since the maximum field of view is typically less than 60 μm. This challenge of multiple length scales is not unique to XCT, with laser diffraction lenses also able to work well at either of the size scales, but not both simultaneously. Recently, correlative tomography has emerged as a valuable tool for combining information from imaging at different length scales [25,26], but as yet, has not been applied to analyse powder samples.

In short, the characterisation of pre-aerosolised inhalation powders remains an unresolved but important question for understanding the performance of inhalation medicines. Despite wide interest in XCT as a potential technique for answering this question, its applicability to inhalation powders remains to be demonstrated. To this end, we characterise the pre-aerosolised 3D microstructure of a representative inhalation blend using multi-scale and correlative XCT, revealing the drug-excipient distribution from bulk-powder scales to individual clusters within the powder sample. This workflow establishes a method for comparing between and within formulations.

2. Materials and methods

2.1. Raw materials

Inhalation grade alpha lactose monohydrate (true density 1.54 g cm^{-3}), namely Lactohale 100 was donated by DFE Pharma (Germany), whilst micronised Fluticasone Proprionate (micFP, true density 1.37 g cm^{-3}) was purchased from Coral Pharma (India).

2.2. Scanning Electron Microscopy (SEM)

SEM was used for the investigation of particle morphology. The powders were deposited onto adhesive carbon tabs (Agar Scientific G3357N), which were pre-mounted onto aluminium stubs (Agar Scientific JEOL stubs G306). Samples were then sputter coated with gold (Quorum SC7620) for 1 min to achieve a thickness of around 30 nm, with images acquired using a JEOL 5700 scanning electron microscope. For the raw material, the microscope was operated at 20 kV. Images were acquired at 100× magnification for LH100 and 500× magnification for micFP. For the blend, the instrument was operated at 10 kV with images acquired at 50×, 200× and 350× magnifications. Note that the micFP used in the SEM images was stored at 0% relative humidity.

2.3. Laser diffraction

Particle size measurements were performed on a Sympatec HELOS/RODOS Laser Diffraction (LDA) unit, equipped with the ASPIROS dispersing system (dispersing aperture diameter 4 mm, feed velocity 25 mm/s) (Sympatec GmbH, Clausthal-Zellerfel, Germany). The R5 lens (measuring range 4.5 μm to 875 μm) was used for both the coarse lactose and the blend whilst the R2 lens (measuring range 0.45 μm to 87.5 μm) was used for micFP. The relative humidity for storage of micronised FP was 10%. In brief, powder was filled into the ASPIROS glass vials and was dispersed via vacuum suction at 0.2 bar, with measurements collected in triplicates. Particle size distributions (PSDs) were calculated using the Fraunhofer theory and were analyzed using the WINDOX 5.3.1.0 software. Results correspond to the mean value of the replicate measurements.

2.4. Blend preparation

A representative inhalation blend was created with Lactohale 100 as the lactose carrier and 10% w/w micFP as the API fines. This is equivalent to 11.1% V/V. The blend was prepared in a Hosokawa high shear mixer fitted with a Picomix module. The lactose carrier was first mixed for 1 min at 1000 rpm, after which the API fines were added and the mixture was mixed for an additional minute at the same rotation speed.

2.5. X-ray Computed Tomography (XCT) data acquisition

2.5.1. Micro-XCT

The blend powder was placed in a 2 mm diameter Kapton tube sample holder [27], with a small segment of paper glued to the top of the tube to act as a lid. The powder was XCT scanned in a Zeiss Xradia Versa 520 XRM instrument, which is a polychromatic, cone-beam, cabinet based laboratory micro-XCT instrument. A voltage of 40 kV and a power of 3 W were used, with a source to sample distance of 9.0 mm and a sample to detector distance of 8.5 mm. 1601 projections were acquired using a 20× objective lens with an exposure time per projection of 12.5 s and 2× camera binning. The effective pixel size was 0.68 μm. The projections were reconstructed into a virtual volume through the proprietary Zeiss Reconstruction software on the XRM instrument, using the FDK algorithm for cone-beam tomography [28].

2.5.2. Nano-XCT

Unblended micFP was loaded into a 500 μm diameter Kapton tube

sample holder [27], with a paper lid glued to the top of the tube. The sample was mounted and XCT scanned in a Zeiss Xradia Ultra 810 XRM instrument, which is a laboratory nano-XCT microscope operating at a photon energy of 5.4 keV. The source operates at 35 keV and 0.9 kW. As the sample was rotated through 180°, 1001 projections were collected using an exposure time of 60 s and 2× camera binning, using the Zernike phase contrast mode. The effective pixel size was 0.129 μm. The individual projections were reconstructed into a virtual volume using the proprietary Zeiss Deep Recon Pro software, using a deep learning based neural network reconstruction algorithm [29]. The reconstructed volume has reduced noise and image artefacts compared with a filtered back projection reconstruction algorithm [29,30].

2.5.3. Correlative XCT

Blend powder was loaded into a 250 μm diameter Kapton tube sample holder [27], with a paper lid glued to the top of the tube. The sample was mounted in a bespoke instrument mount that was designed for easy transfer of samples between Zeiss Xradia Versa XRM and Zeiss Xradia Ultra XRM instruments. The sample was first micro-XCT scanned in a Zeiss Xradia Versa 520 XRM instrument, using a coarse resolution of 3.65 μm to cover the entire sample (scan 1). Higher resolution micro-XCT scans at 0.74 μm were then performed at several regions of interest, including one covering the top of the metallic pin within the sample mount (scan 2) and another within the bulk of the powder (scan 3). All of these micro-XCT scans on the Zeiss Versa XRM instrument had source to sample and sample to detector distances of 10 mm and 8.5 mm respectively, camera binning of 2× and 1601 projections acquired as the sample was rotated through 360°. The remaining micro-XCT scan details are provided in Table 1. The raw projections were converted to virtual volumes as in Section 2.5.1. The sample was then transferred to a Zeiss Xradia Ultra 810 XRM instrument, taking care to minimize any powder disturbance. Several nano-XCT scans were acquired, including at the top of the metallic pin and within the powder bed. Compared to the micro-XCT scans, the nano-XCT scans were at a higher resolution but over a smaller region of interest. The nano-XCT scan settings are provided in Table 2. The raw projections were converted to virtual volumes as in Section 2.5.2.

2.6. Image analysis

2.6.1. Micro-scale data

A single slice through the raw, unprocessed micro-XCT virtual volume of the blend is shown in Fig. 1A. The virtual volume for the blend was first processed with the proprietary phase removal filter PhaseEvolve (Zeiss Microscopy, CA), which removes phase fringes and reveals the underlying subtle differences in absorption, as can be seen in Fig. 1B. A short explanation of the physics behind this filter is provided by Andrew et al. [29] with the effect of the filter illustrated in the supplementary material. This phase-filtered volume was then loaded into Avizo 2020.2 (Thermo Fisher Scientific, France) for further image processing using built in modules sequenced as a Tcl script. The image was cropped to an internal cylindrical region of interest, before segmenting into air, drug-rich and carrier lactose phases using a 3-phase automatic Otsu thresholding algorithm [31], as shown in Fig. 1C. The local thickness of the drug-rich phase (Fig. 1D) was calculated using the thickness map algorithm [32], which, for each voxel, calculates the maximum radius of a cylinder centred at that voxel completely enclosed within the drug-rich phase (Fig. 1E). Intermediate volume files and statistics produced by Avizo were wrangled using Matlab to produce data that could be further processed using the opensource statistics and data science language R [33], version 4.1.3. All of the final statistics were wrangled and visualised using R, including the total percentage of drug-rich phase and lactose within the entire analysis volume, and the distribution of drug-rich phases thicknesses across all of the identified drug-rich voxels within the volume. The percentages of drug-rich phase and lactose within each slice were also calculated, using a sliding mean over 30 μm to smooth over the arbitrary virtual slicing of the powder bed.

The blend powder bed was also split into individual clusters (containing drug-rich phase, lactose and air) by first filling all holes and then using a standard watershed based separation algorithm [34,35]. The strength of the split parameter was calibrated by visual inspection to prevent under- or over-splitting, as well as comparing the resultant size distribution with results from laser diffraction. The clusters touching the edge of the analysis cylinder were removed, with 329 clusters remaining for further analysis. The clusters in the visualised slice are shown in Fig. 1F. The clusters were filtered before further analysis with those clusters having a maximum thickness less than 2.04 μm (3× the effective pixel size) removed, leaving 119 clusters.

For analysis of each cluster, the total volume of the cluster, as well as the volumes of the respective drug-rich, air & lactose phases within each cluster were determined. The diameter of a sphere with a volume equivalent to the total volume of the relevant phase was calculated (i.e. the equivalent spherical diameter). The lactose volume measurement is the sum total of lactose within the cluster, and therefore the lactose equivalent diameter cannot distinguish between whether there is a single lactose crystal or multiple lactose crystals within the cluster. The volumes for each phase within each cluster were used to calculate the proportions of the drug-rich phase and lactose.

A selection of distribution statistics (minimum, maximum, mean, median and quantiles) for the drug-rich phase thickness within each cluster were calculated. Additionally, the minimum (Euclidean) distance of each drug-rich phase voxel within a cluster from the cluster boundary was calculated, with the distribution statistics summarised for each cluster. Similarly, the minimum (Euclidean) distance of each drug-rich phase voxel within a cluster from the lactose phase calculated (irrespective of whether the lactose is within the cluster or outside), with the maximum such distance summarised for each cluster.

Additional 2D and 3D visualisation was performed in Dragonfly Pro 4.1 (Object Research Systems, Canada).

2.6.2. Nano-scale data

The virtual volume was loaded into Dragonfly Pro 2020.1 (Object Research Systems, Canada) for visualisation.

2.6.3. Correlative data

All of the correlative micro-XCT and nano-XCT datasets were loaded

Table 2
Scan parameters for correlative nano-XCT scans performed on the Zeiss Xradia Ultra 810 XRM instrument.

Location	Camera binning	Projections	Exposure time (s)	Pixel size (μm)
Pin	2×	801	60	0.129
Powder	2×	801	60	0.129
Powder	1×	1601	150	0.064

Table 1
Scan parameters for correlative micro-XCT scans performed on the Zeiss Xradia Versa 520 XRM instrument.

Scan	Description	Objective magnification	Voltage (V)	Power (W)	Exposure Time (s)	Effective pixel size (μm)
1	Coarse full-field of view	4×	80	7	0.5	3.65
2	ROI pin	20×	110	10	6	0.74
3	ROI powder	20×	40	3	12.5	0.74

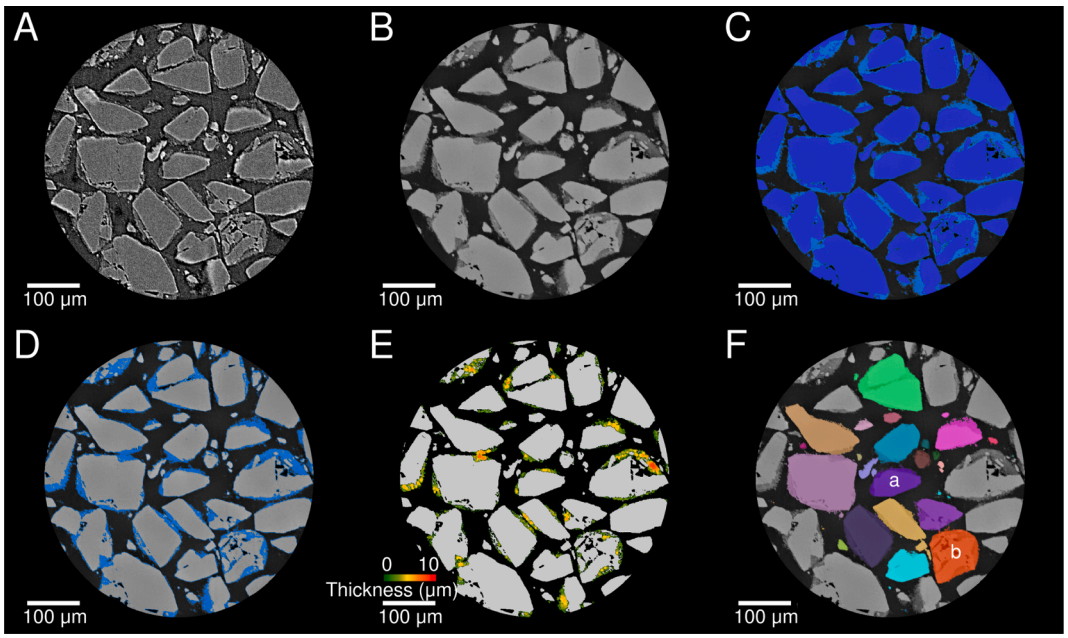

Fig. 1. One individual micro-CT slice taken from the virtual volume, viewed in different ways: (A) Raw data; (B) after phase filtering; (C) colour washed with segmentation of lactose (dark-blue) and drug-rich (light-blue) phases; (D) colour washed with only rich-phase phase; (E) local thickness map of the drug-rich phase; (F) colour washed with individual separated clusters. Particles labelled (a) and (b) in (F) refer to the clusters with the two example structures detailed in Fig. 9.

into Dragonfly Pro 2020.1 for alignment and visualisation. The pin was used as a point of reference to convert the micro-XCT datasets to the same coordinate system as the nano-XCT datasets, with further fine alignment performed manually by matching common features (e.g. lactose to drug-rich phase interfaces) within scans.

2.7. Modelling the drug-rich phase fraction

A mathematical relationship linking the fraction of drug-rich phase to the thickness of the drug-rich phase was derived in the following manner. By definition, the drug-rich fraction for a cluster is the proportion of the total cluster volume which comprises the drug-rich phase. The volume of the cluster can be written as $\frac{4}{3}\pi r_{\text{cluster}}^3$, where the equivalent spherical diameter $d_{\text{cluster}} = 2r_{\text{cluster}}$. Similarly the total volume of lactose within a cluster can be written as $\frac{4}{3}\pi r_{\text{lactose}}^3$, with the equivalent lactose spherical diameter $d_{\text{lactose}} = 2r_{\text{lactose}}$. Since $r_{\text{cluster}} \geqslant r_{\text{lactose}}$, say that $r_{\text{cluster}} = r_{\text{lactose}} + x$, where x is the thickness of the drug-rich phase. It is assumed that x is related to the amount of lactose in a cluster, i.e. $x = f(r_{\text{lactose}})$ for some function f, thus the fraction of drug-rich phase is given by (1).

$$\text{Drug-rich phase fraction} = \frac{(r_{\text{lactose}} + x)^3 - r_{\text{lactose}}^3}{(r_{\text{lactose}} + x)^3} \quad (1)$$

3. Results

3.1. Raw material characterisation

The raw materials used in the blend are shown in Fig. 2. Visually, both the SEM and XCT images show the different length scales and textures of the carrier LH100 lactose (Fig. 2A) and micFP (Fig. 2B). The LH100 comprises individual particles approximately 100 µm in size, with a characteristic tomahawk lactose shape [16,27,36], whilst the micFP comprises a very fine powder of the order of microns in size. These differences in length scales are also evident in the laser diffraction size distribution summarised in Table 3. The nano-XCT images in Fig. 2B also show the cohesive nature of micFP, with many small particles (light regions) grouped closely together with small air pockets in between

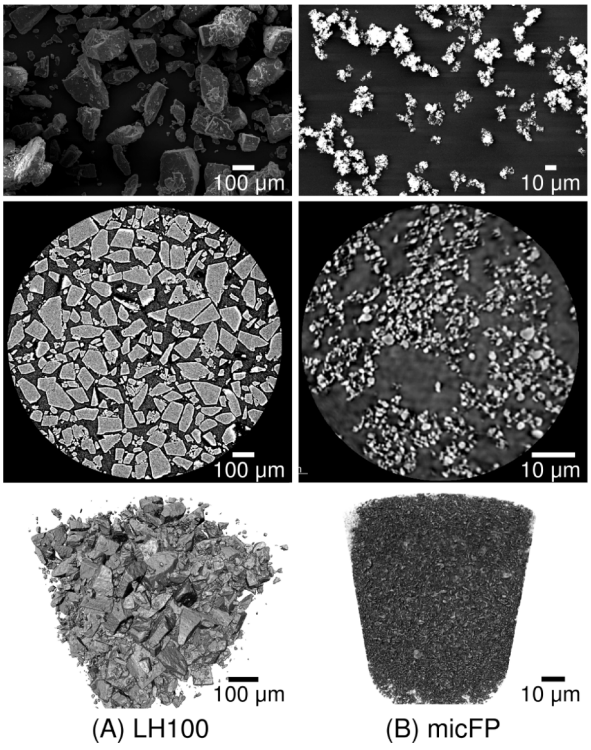

Fig. 2. (A) LH100 carrier lactose and (B) micronised FP represented as SEM images (top), virtual 2D slices through the XCT virtual volume (middle) and XCT volume renderings (bottom). Note the different scales for the two materials, with XCT data acquired by micro-XCT and nano-XCT in (A) and (B) respectively.

(dark regions) forming regions of high drug density. This cohesive nature can also be seen in the SEM image in Fig. 2B as small clusters with high drug density, but the dispersion in SEM preparation means that the distance between the clusters is greater than for XCT, where the powder

Table 3
Size distribution of raw micronised FP and raw lactose from laser diffraction.

Material	Size measurement (μm)		
	d10	d50	d90
Raw LH100	59	135	226
Raw micFP	5	23	37
10% micFP blend	48	140	231

is imaged in its native state without any additional dispersion.

3.2. Bulk powder characterisation

Table 4 shows the void fraction to be 35% with Fig. 3A showing variations in powder density (and thus void fraction) as a function of height through the packed powder sample. This is lower than previous micro-XCT measurements for tabletting grade lactose and for LH100 [16], highlighting that the blend has a more compact packing. The small variations in powder volume are due to different sized particles.

The d50 and d90 particle size measurements in Table 3 show that the size of the blend is only slightly larger than raw LH100, showing that the addition of micFP has not significantly altered the particle size distribution. Laser diffraction measurements were performed at the lowest practical dispersion pressure (0.2 bar) in an attempt to maintain the native agglomeration state of the powder during measurement for comparison to the powder bed XCT size distributions. The full size distribution is shown in Fig. 3B. Although dispersed at 0.2 bar, there is still a small tail of fine particles at the left of the distribution, showing that some fine drug particles have been separated during the measurement. This separation of fine particles also means the d10 value in Table 3 is lower for the blend compared to LH100 alone. The size distribution measured by micro-XCT has a maximum peak at a much smaller size, with a second peak around 100 μm; however this second peak is likely to be an artefact of the very small number of particles considered. Previous work [16] showed micro-XCT to report smaller particle sizes since it is a fully 3D technique measuring the actual volume of non-spherical particles. This contrasts with laser diffraction that calculates an equivalent sphere diameter based on the diffraction angle of incident laser light. Fig. 3C shows the distribution of cluster sizes across the height of the sample. Although the smaller-sized particles and drug-containing clusters are distributed fairly equally across the height, larger clusters are concentrated towards the middle of the sample. Any large cluster lying closer to the top or bottom is likely to cross the boundary of the analysis cylinder, and hence would be only partially imaged. These particles are thus excluded from the analysis.

3.3. Microstructural characterisation of the blend

The raw micro-XCT data and phase-filter processed data in Figs. 1A, B show two distinct phases, with a less dense layer surrounding more dense particles. The difference in density was sufficient to allow thresholding into the separate phases in Fig. 1C, with the identified micFP-rich phase shown in Fig. 1D. The correlative XCT datasets allow further examination of these identified phases, with the full micro-scale field of view shown in Figs. 4A, B. The corresponding region of interest of the same sample imaged using nano-XCT is shown with the blue box in Fig. 4. At micro-scale resolution, there are clearly three greyscale phases as shown in Fig. 4C, but the nano-XCT virtual slice of the same region shows that the drug-rich phase (micFP) has a very similar powder texture to raw micFP (Fig. 2B). At the high resolution, this phase can be seen to comprisedrug particles and air pockets that are of similar length scales, and hence is referred to as the 'drug-rich' phase. Thus the nano-XCT slice confirms the greyscale segmentation of the micro-XCT data into lactose, drug and air phases.

Table 4
Bulk statistics for 3 identified phases (air, lactose and drug-rich measured by micro-XCT). The volume of one voxel is equal to one pixel cubed ($0.68^3 \mu m^3$).

Phase	Number of voxels (millions)	Percentage of total volume (%)	Percentage of powder volume (%)
Air	138	35	-
Lactose	210	54	83
Drug-rich	42.6	11	17

Table 4 shows the number of identified voxels in the micro-XCT data for each phase, and their proportion of the total volume and powder volume. The total volume of drug-rich areas identified by micro-XCT is quantified at 17% of the powder volume, which is higher than the proportion of drug within the blend (10% w/w and 11.1% V/V). A possible explanation for this discrepancy is partial volume effects. As can be seen in Fig. 4D, the drug-rich phase contains both drug particles and air, and thus the identified drug-rich volume is greater than the actual volume of drug particles alone. Fig. 3B shows that the drug-rich region to lactose ratio is fairly consistent throughout the height of the powder bed.

Fig. 5 shows 3D visualisations of the blend from micro-XCT. Fig. 5A shows a 3D cutaway visualisation of the blend, with the drug-rich phase coloured according to its thickness as calculated using the thickness algorithm [32], whilst Fig. 5B shows the same 3D cutaway with each cluster given a different random colour. SEM images of the same blend (at a different time point after blending) are shown in Fig. 6. At the lowest resolution (Fig. 6A), it is not possible to distinguish the drug from the carrier lactose. The intermediate magnification (Fig. 6B) shows evidence of the micronised FP coating the lactose carrier, although not all facets are visible for all particles. The highest resolution (Fig. 6C) shows this coating in higher detail, with individual drug particles identifiable. The cluster in the middle of the latter image (marked by a white arrow) appears to indicate an aggregated structure comprised of several lactose particles with micronised drug particles. However, the view is obscured by the micronised drug coating the surface of the cluster as well as the image being only two-dimensional, so it is not possible to determine the exact structure.

The distribution of the local thickness of the drug-rich phase throughout the micro-XCT analysis region is shown in Fig. 7. Three quarters of the voxels have a thickness less than 2.5 μm, whilst the mean thickness is 1.9 μm. This indicates that a significant fraction of the blended API has formed a tightly packed coating around the larger 'carrier' lactose particles. There are also a number of voxels with thicknesses greater than 5 μm (distribution outliers), with a small number displaying thicknesses greater than 10 μm. This is consistent with the presence of larger drug agglomerates that possess a large volume of the powder bed within a given cluster region.

3.4. Microstructural characterisation of individual clusters

The individual separated clusters are shown 2-dimensionally and 3-dimensionally in Figs. 1F and 5B respectively. Quantitative assessment of each of the clusters is shown in Fig. 8. Fig. 8A shows that as the amount of lactose in each cluster increases (expressed as the increase in the volume-equivalent sphere diameter of lactose), the mean thickness of the drug-rich phase across the cluster also increases. Although there is variation in the data, a linear model provides an adequate description (Table 5), with tight confidence intervals on the fitted parameters. The adjusted R-squared for the fit was 0.60. Note that the mean thickness for the drug-rich phase calculated over the entire analysis region (without cluster information), shown with the dotted line, overestimates the thickness; this is because larger clusters contribute a greater number of voxels to the overall mean.

Fig. 8B shows that the proportion of drug-rich phase in each cluster is also related to the amount of lactose in each cluster. Clusters that are large, as they contain a large total volume of lactose, have smaller proportions of drug-rich phase. There are some very small clusters

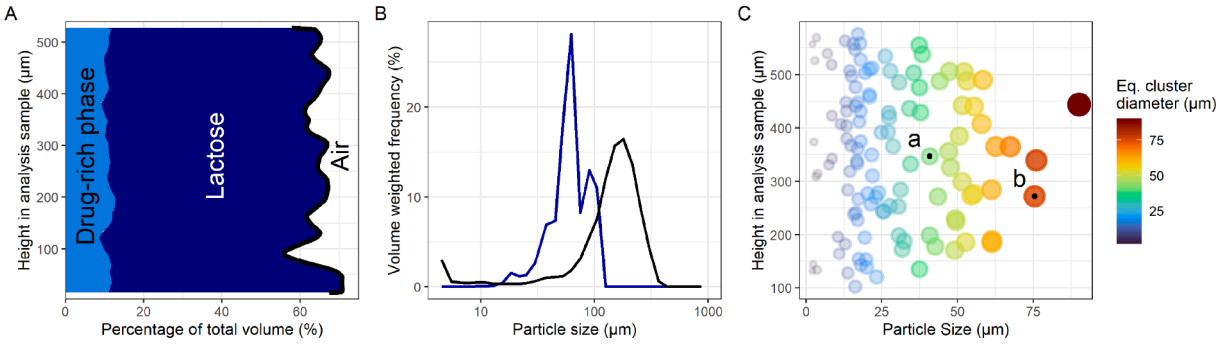

Fig. 3. (A) Total volume fractions of drug-rich phase, lactose and air as a function of height, showing proportion of powder which is lactose and which is drug-rich. (B) Powder size distribution for the blend as measured by laser diffraction at 0.2 bar (black) and micro-XCT (dark blue). (C) Relationship between cluster 'particle' size and height. Clusters labelled (a) and (b) refer to the two example structures detailed in Fig. 9.

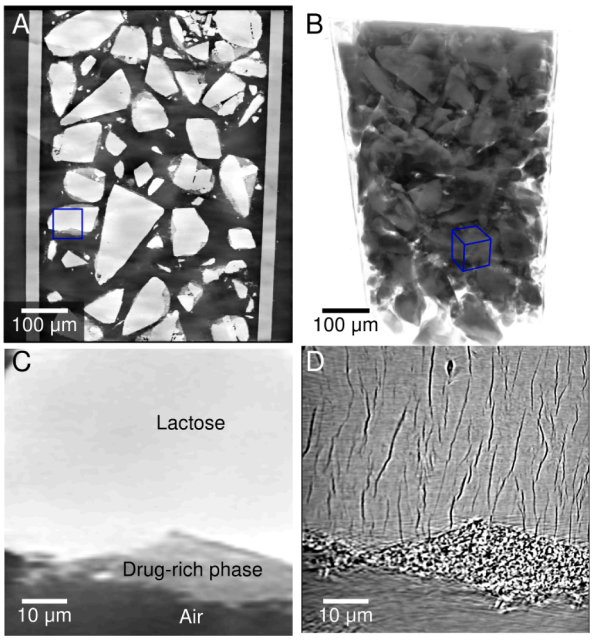

Fig. 4. A comparison of the lactose and drug-rich regions through correlative XCT: (A) A virtual vertical slice through the entire sample scanned with micro-XCT with the region of interest for nano-XCT marked in blue; (B) A 3D rendering of the entire sample, from micro-XCT. The region of interest for nano-XCT is marked in blue; (C) Micro-XCT data zoomed to the region of interest; (D) Corresponding correlative nano-XCT of the region of interest.

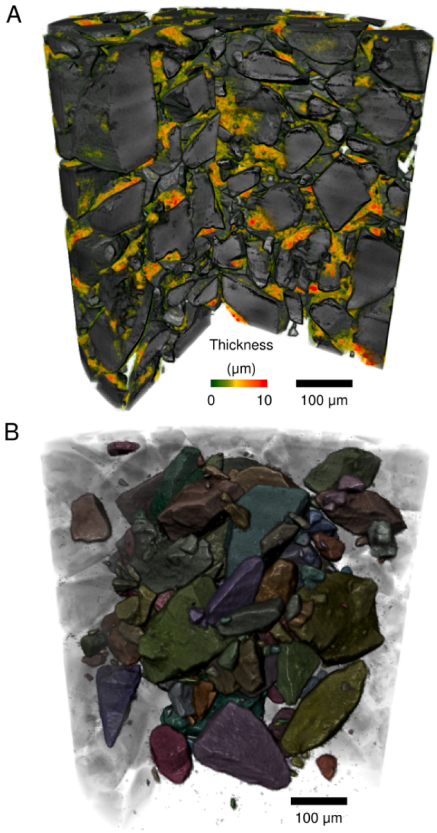

Fig. 5. 3D virtual cutaway visualisations of the blend from micro-XCT: (A) Visualisation with the drug phase coloured according to its local thickness. The color scale is the same as in Fig. 1E. (B) Visualisation of the analysed clusters using a separate random colour for each cluster. The entire blend is shown in the background as semi-transparent.

containing almost 100% drug-rich phase which correspond to fines-only clusters; however if there is lactose in a cluster then the drug-rich phase proportion is below 50%. Eq. (1) together with the linear thickness model of Table 5 is able to capture this inverse relationship between amount of lactose and drug-rich phase proportion, and provides a much better description than a scaling using a constant thickness. In brief, the largest clusters are composed primarily of lactose, and even though large clusters contain the smallest proportion of drug-phase, they possess the greatest drug-phase thickness.

Although the simple mathematical scaling provides a good description, there is variation between the clusters. Fig. 8C also shows that there is variation across a cluster, with the upper 10% of thicknesses in a single cluster having a range of up to 7 μm. The maximum thickness is below 10 μm, with only a single cluster (labelled 'b' and maximum thickness 12.5 μm) having a maximum thickness greater than this limit. Fig. 8D shows that as the amount of the lactose increases, the maximum distance of the drug-rich phase from the cluster boundary also increases, although the figure also shows the variation in this parameter across the clusters. For clearer visualisation of the trends, Figs. 8C and 8D presents only the range 90%-100% for each cluster of both the distribution of thicknesses and distribution distances of the drug-rich phase from the cluster boundary. The full distributions are presented in the Supplementary Material, in Figures S3C and S3D. The cluster size is itself directly proportional to the lactose volume it contains (Supplementary Material Figure S3A), although this provides no indication as to whether a cluster contains a single large crystal or aggregates of smaller lactose crystals within its cluster volume.

Visual inspection (Figs. 1F and 5B) shows that there are a number of different structures with some clusters containing a single lactose crystal whilst others contain multiple lactose crystals with regions of air in-

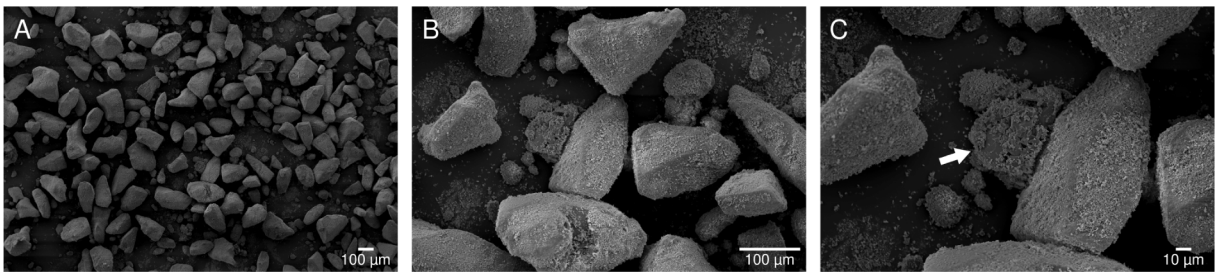

Fig. 6. SEM images of the blend at three different magnifications: (A) 50×; (B) 200×; (C) 350×.

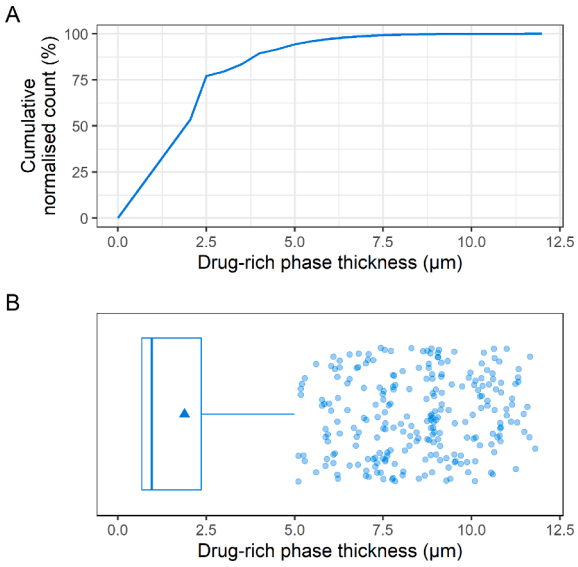

Fig. 7. Two representations of the distribution of drug-rich phase thickness across all identified drug pixels within the analysis region measured by micro-XCT: (A) Cumulative frequency; (B) Box plot, with the mean shown as a triangle marker and distribution outliers shown as circular point markers with vertical jitter to prevent overlap.

between. Two example structures are illustrated in Fig. 9: Structure (a) contains a single large lactose crystal having a classical tomohawk shape, with a second small lactose crystal attached to one of the faces; Structure (b) contains many lactose crystals that have a range of sizes. These 3D visualisations also suggest that the distribution of drug-rich phase across a lactose is heterogeneous, with the drug-rich phase concentrated in certain "drug-rich" parts of a cluster whilst other parts of clusters are "drug-poor".

Fig. 8E shows that the maximum distance from lactose of the drug-rich phase in each cluster generally increases with the amount of lactose in each cluster, before saturating at a distance of ≈ 37 µm. Although structures (a) and (b) are very different, containing differing amounts of lactose, the drug-phase in each structure has a very similar maximum distance from the lactose phase. It can also been seen that the drug-rich clusters (containing very small proportions of lactose) show large variation in the maximum distance from lactose, with a range that is nearly as large as all of the remaining clusters. In summary, these data demonstrate that the small drug-rich clusters have low drug-thickness but may have large distances from lactose voxels (indicating drug agglomerates not associated with carrier), while big clusters contain large volumes of lactose that are co-associated with regions of thick drug-phase. In order to ascertain whether a cluster represents a drug-only agglomerate or carrier-associated drug phase, it is therefore necessary to consider all of the metrics of thickness, drug phase proportion and distance from lactose voxels as a function of the lactose content of the cluster.

4. Discussion

An important part in understanding the microstructure of dry-powder inhaler (DPI) formulations is the ability to characterise the pre-aersolised powder. In this study, we have demonstrated how high resolution X-ray computed tomography (XCT) can be used to analyse DPI powders, without any disturbance or dispersion. Using micro-XCT, we revealed the 3D spatial distribution of phases (air, lactose and drug-rich phase) across a model inhalation DPI blend, with correlative nano-XCT used to validate the phase identity. Although it is accepted that API concentrations as high as 10% w/w are uncommon in marketed inhaled products, DPI blends typically contain 10-20% of fine particles when the mass of API and intrinsic or extrinsic carrier fines (e.g. micronized lactose) are combined. For this reason 10% w/w of micFP was employed as a single component of fines within the blend for the current study. The 3D spatial information allowed the lactose-drug relationship to be analysed at multiple scales, from the bulk scale down to the particulate level.

Comparing the powder bed with other powders analysed using the same micro-XCT technique, the inhalation blend has a higher powder volume fraction than L-glutamic acid [15], tabletting grade lactose [16] or LH100 alone [16]. This implies that the addition of the drug allows a close packing between the individual units within the powder blend. Close packing of powder beds with air spaces interstitial to the larger carrier particles being occupied by agglomerative masses of extra-fine particles has been hypothesized to occur in the DPI carrier blends [37], serving as a barrier to air permeation and blend fluidization during aerosolization [38]. This work has demonstrated such close packing within an undisturbed powder bed.

Although the material densities of carrier lactose (1.54 g cm^{-3}) and the drug fluticasone propionate (1.37 g cm^{-3}) are similiar, it is encouraging that there is sufficient contrast on laboratory micro-XCT instruments to differentiate between the drug-rich phase and the carrier excipient. Micro-XCT cannot by itself identify the chemical species, but the first application of correlative XCT to the same sample provides validation of the drug-rich phase coating the carrier lactose since the drug-rich phase within the blend has a similar texture to nano-XCT of the drug alone. Notably, the blending process compressed the drug particles into a higher density phase, and this can be seen compared to the nano-XCT of the drug alone. The correlative XCT datasets also highlight the partial volume effects within the micro-XCT scan, with a single voxel at a resolution of 0.68 µm covering both nano-sized drug particles and air. Interestingly, the correlative nano-scale image of the blend in Fig. 4D reveals distinct cracks within the lactose particles. Cracks were previously seen in a different lactose grade [24], and work is underway to understand whether the orientation of the cracks is a feature of the lactose morphology or a result of the crystallisation process, and whether the cracks have any influence on blend performance [39]. The correlative XCT technique demonstrates how different length scales can be analysed simultaneously, and this could provide new 3D insight into other pharmaceutical products such as coated granules [40].

Whilst there are a number of techniques for exploring inhalation formulation microstructure, none of the existing techniques give 3D

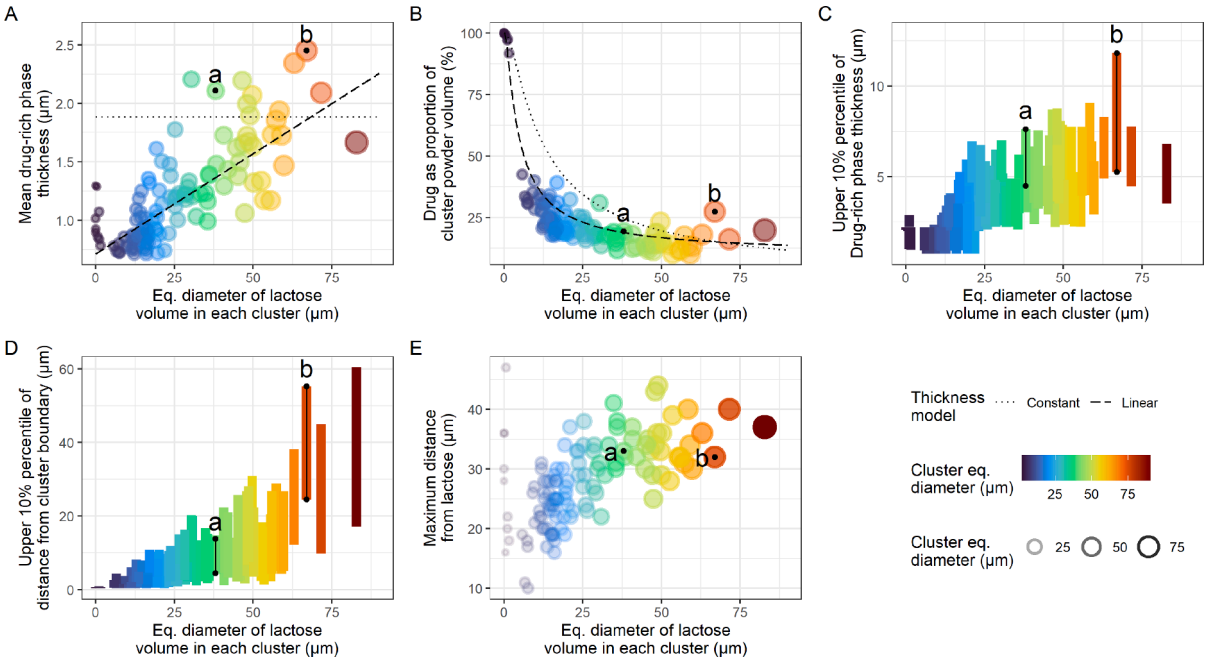

Fig. 8. Individual statistics for each identified cluster, as measured by micro-XCT. Clusters labelled (a) and (b) refer to the two example structures detailed in Fig. 9. (A) Relationship between the mean thickness of the drug-rich phase in each cluster and volume of lactose in each cluster. The lactose volume is expressed as the equivalent spherical diameter of the cumulative volume in a cluster. Dotted and dashed lines show constant and linear relationships respectively; (B) Proportion of identified drug-rich phase within each individual cluster. Dotted and dashed lines are scalings from Eq. (1) using the constant and linear thickness models; (C) Upper 10% quantile of drug-rich phase thicknesses within the cluster; (D) Upper 10% quantile of distances of drug-rich phase from cluster boundary; (E) Relationship between the maximum distance of the drug-rich phase from lactose and the volume of lactose in each cluster.

Table 5
Linear regression parameters for the relationship between equivalent diameter of lactose in each cluster and mean thickness for the drug-rich phase in each cluster measured by micro-XCT.

Parameter	Value (95% CI)
Intercept	0.71 (0.63, 0.80)
Slope	0.017 (0.015, 0.020)
Residual standard error	0.259
Adjusted R-squared	0.598

spatial information. Figs. 5 & 6 compare the XCT method from this study with the current imaging standard of SEM, with the XCT results demonstrating a new level of detail. First, the XCT technique is able to differentiate between the drug-rich and lactose phases, but furthermore, it can also visualise both the drug-rich phase thickness (Fig. 5A) and individual lactose-drug clusters (Fig. 5B). Furthermore, it provides the full spatial relationship of the distribution of the blend components throughout the packed powder bed, exactly as it exists in the bulk powder. These results are truly 3D in nature, and from a purely qualitative view point, provide richer morphological insight compared to SEM. For example, although high-magnification SEM in Fig. 6 reveals the drug-rich coating, the coating obscures the structure underneath. In contrast, Fig. 9 shows visualisations of the lactose structure underneath the drug-rich coating. Importantly, XCT data also allows for quantitative analysis, with the bulk distribution of drug-rich phase thickness shown in Fig. 7 and individual statistics for each cluster shown in Fig. 8. This not only provides a high level of scrutiny of the blend microstructure, but also provides a means for comparing the microstructure of the different powder blends. For example, Fig. 8A and Table 5 show how the drug-rich phase thickness scales with the lactose content of the cluster, expressed as the equivalent sphere diameter size of the lactose volume in the cluster. Studies are ongoing to examine whether this scaling is constant for all drug-excipient combinations, or whether the scaling changes for depending on the particular API-excipient combination.

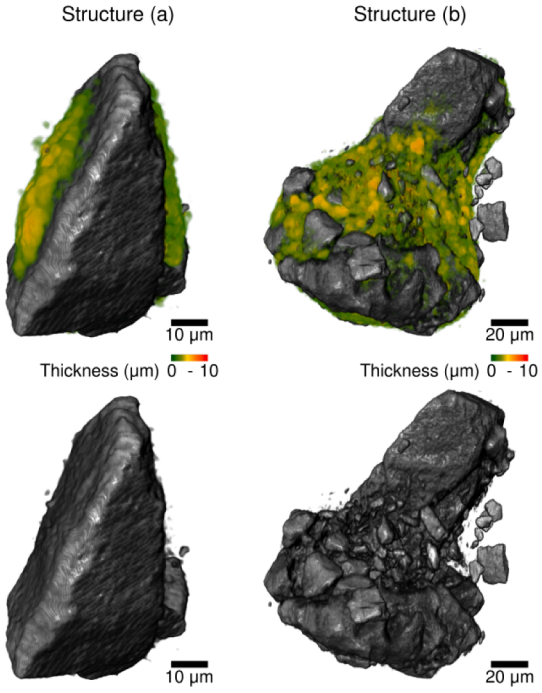

Fig. 9. Two example volume renderings of individual particle structures obtained by micro-XCT for illustration: (a) A single LH100 carrier particle with a smaller lactose particle attached to one facet, and micFP adhered to certain facets; (b) Several LH100 particles bound together in a single cluster, with micFP located in between the carrier particles. The top panels show visualisations of the entire cluster, with the drug phase rendered according to its thickness using the same colour scale as Fig. 3E, whilst the bottom panels show visualisation of only the lactose part of each structure.

Inhalation blends are traditionally considered classical examples of "ordered mixtures" [41], in which the drug-carrier distribution is completely homogeneous. This is despite the fact numerous observations demonstrate the presence of cohesive drug agglomerates within blends, that have limited interaction with the carrier particles [e.g. 42–45]. Fig. 3A shows the drug-rich phase to lactose ratio to be homogenous on a bulk scale. The concept behind a theoretical "ordered mixture" is specific units where the drug has adhered evenly to the excipient. In practise, identification of such units is very challenging without powerful visualisation methods. The 3D analysis in this work allowed identification of drug-lactose clusters, which were different sizes (Fig. 3C) and contain a different proportion of drug-rich phase depending on the size of the cluster (Fig. 8C). The cluster size was directly proportional to the lactose content of the cluster, and drug-rich phase proportion scaled with the volume of carrier. The latter was also illustrated by the thickness-lactose size relationship (Fig. 8A), which is different to the surface area scaling proposed by Hersey [41].

The 3D analysis in this work also allows the carrier to drug-rich phase to be visualised and quantified across the entire blend. Rudén et al. [46] hypothesised that at low concentrations of fine particles, the fine particles fill in crevices in the carrier particles. At higher concentrations of fine particles, the fine particles combine at the surface of carrier particles causing an increase in the envelope of the aggregated particles. Rudén et al. [46] also described that the fines population may also exist as 'free-fines' without the presence of carrier particles. Both of these populations of fine particles were visualised in Fig. 5 and quantified in Fig. 8. Whilst [46] reported that significant 'free-fines' were present for concentrations of micronised lactose above 10.9% w/w, Fig. 8 shows that for 10% w/w micronised FP, the majority of fine particles exist adhered to carrier particles and only a very small population of free micronised FP fines exists. This difference in behaviour between the micronised FP - carrier blend in this study and micronised lactose - carrier blend used in [46] points towards differences in the adhesive-cohesive behaviour between the two fines populations.

Fig. 9 shows that the clusters also possess different structures, with some clusters containing single carrier particles (Structure (a)), whilst others contain many carrier particles bound together with the drug-rich phase (Structure (b)). This demonstrates a level of heterogeneity across the sample, challenging the notion of the inhalation blend being an 'ordered mixture'. While we have shown the relationship between drug-phase thickness and cluster size/lactose content, the metrics do not clearly reveal by themselves whether the lactose volume is composed of a single large carrier crystal, or multiple smaller crystals in an aggregate structure. By interpolating between the metrics of cluster size, lactose volume and porosity of the cluster (air volume content shown in the Supplementary Material in Supplementary Figure S3B) it does appear that clusters composed from agglomerated drug/carrier crystals (Structure (b)) can be distinguished from individual carrier particles coated with drug (Structure (a)). Machine learning techniques could be utilised in characterising each cluster based on the number of carrier particles, but such analysis lies outside the scope of this work. As well as understanding how these cluster structures form, the information obtained from XCT advocates strongly for the future use of the technique to examine the relationship between the presence of these complex cluster structures containing multiple carrier particles and the aerosolisation behaviour, and thus the performance of the inhalation blend.

Furthermore, even for single carrier structures, the distribution of drug-rich phase across the carrier is not homogeneous. Structure (a) in Fig. 9 shows facets pointing out of the page do not contain any drug-rich phase, whilst the facets on the left and right of the crystal contain significant amounts of drug-rich phase. Understanding the relation between the drug-lactose binding and the crystal chemistry is invaluable to predicting cluster structure formation but also the blend performance through predicting the energy needed to detach the drug from the carrier. Molecular modelling studies similar to Gajjar et al. [18] and Nguyen et al. [19] are currently underway to understand the facet-specific drug-carrier binding, and the experimental visualisation in this study of the individual units will be invaluable alongside those modelling results.

The maximum distance of the drug-rich phase from the lactose phase for each cluster shown in Fig. 8D, showing the maximum distance saturates around 37 μm may also be another characteristic that is dependent on the particular drug-carrier interactions for the blend. This statistic provides both micro-, and macro-structural information of the blend, indicating how individual clusters are structured, but also how the phases within different clusters interact with each other. Such statistical analysis clearly lends itself to the examination of different blend compositions, as it may provide another measure for uniquely identifying particular formulation behaviours.

One limitation of this study is the small analysis volume. The final cylindrical analysis volume, after cropping to remove edge artifacts, was 0.123 mm^3, with 0.066 mm^3 of lactose and an identified drug-rich phase volume of 0.013 mm^3. For content uniformity, the same amount as the unit dose of formulation would need to be analysed. Thus, if a similar requirement was placed for micro-XCT, a typical 20 mg dose would require roughly 1000 samples to be analysed. This is difficult, but becoming more feasible with a recent developments in deep learning based reconstruction and image analysis methods coupled with developments on the hardware side to enable automation in sample loading and scanning [30]. On the other hand, TOF-SIMS is an imaging technique used for quantifying the surface composition and surface structure, but as the imaging window is 500 μm × 500 μm at low resolution and 50 μm × 50 μm at high resolution, typically only a few particles are analysed. Defining acceptable sample volumes for XCT will requiring the weighing up of the large time and cost of scanning a representative amount of material against the rich blend information provided by a single scan.

Only 119 particles remained in the analysis after excluding particles not fully within the analysis cylinder, with larger particles more likely to lie across the boundary and thus be removed. This bias is one reason that the blend size distribution shown in Fig. 3C shows a higher proportion of small particles. Typically, 2000-3000 particles is considered the minimum for a balanced distribution, with the analysis in this study one order of magnitude lower. Further studies are needed to validate the method across a larger analysis volume and larger number of particles. This would be a combination of multiple samples from the same blend, multiple regions scanned within the same sample, and larger stitched scans covering a larger volume to increase the likelihood of including large particles in the analysis. With circa 6 hours needed for each scan, the time-per-particle ratio is very high. Further work is needed on the instrument-side to reduce this, which may involve a combination of hardware improvements and machine-learning approaches to extract rich information from more limited data.

Further work is underway to use this method to assess differences in blend composition and blend evolution over time. Furthermore, work is underway to examine the relationships between microstructure and aerosolization performance. In the current study, we have reported the development of the XCT analytical technique and image analytical workflows to define metrics for microstructural comparison. Nevertheless, it is still necessary to examine the sensitivity of the method to detect subtle differences in formulation, or intra- and inter- batch variability. Studies are on-going in this area. Having demonstrated the method with binary API-lactose blends, it is also essential to examine the sensitivity of the method to distinguish between tertiary or still more complex blends typically seen in licensed products. Given sufficient data (over many blends and replicates), the advancement of AI and machine learning techniques may allow deeper evaluation into microstructural differences present. This work is a first step in assessing potential metrics for microstructural characterisation, and allows human insight into the technique that is valuable for designing future studies.

Overall, despite the limitations, this study demonstrates new 3D insight into the microstructure of pre-aerolised DPI powders, and in

doing so, opens new doors to bioequivalence assessment of inhalation formulations.

5. Conclusion

Characterising the pre-aerosolisation powder microstructure of inhalation blends is vital for understanding post-aerosolised performance. In this study, we have employed novel correlative multi-scale X-ray computed tomography to examine the microstructure of an inhalation blend. Carrier lactose and drug-rich regions were identified on a micro-scale and validated by comparing against raw drug at nano-scale resolution. The drug distribution was analysed from bulk to individual cluster scales, showing that whilst drug-lactose proportions are homogenous on a bulk scale, they are heterogeneous on an individual particular scale. A simple linear relationship between the thickness of the drug-rich phase and the lactose in a cluster could predict the drug proportions of each cluster. In conclusion we report a new analytical technique and approach for characterisation of bulk powder microstructure in pre-aerosolized formulations for drug delivery to the lung.

License Statement

Data Access

Additional research data supporting this publication may be available on request to the authors.

Declaration of Competing Interest

The authors declare that they have no known competing financial interests or personal relationships that could have appeared to influence the work reported in this paper.

Data availability

Data will be made available on request.

Acknowledgements

The authors of this paper were all part of the INFORM2020 consortium, which was funded through EPSRC grant EP/N025075/1. We are grateful to consortium partner DFE Pharma and to Meggle for providing the raw materials. We further acknowledge Kindeva Drug Delivery, Astra Zeneca, Glaxo Smith Kline, Malvern Panalytical and Carl Zeiss Microscopy for their membership and support of the INFORM2020 consortium. PG is grateful for support from colleagues at Seda Pharmaceutical Development Services in completing this work. PG also acknowledges support from EP/M010619/1. PJW acknowledges funding from an ERC advanced grant Correl-CT (No. 695638). Beamtime for this study was kindly provided by the Henry Moseley X-ray Imaging Facility (HMXIF), which was established through EPSRC grants EP/F007906/1, EP/I02249X/1 and EP/F028431/1, and is now part of the National Research Facility for Laboratory-based X-ray CT (NXCT), funded through EPSRC grant EP/T02593X/1. HMXIF is also a part of the Henry Royce Institute for Advanced Materials, established through EPSRC grants EP/R00661X/1, EP/P025498/1 and EP/P025021/1.

Appendix A. Supplementary material

Supplementary data associated with this article can be found, in the online version, at https://doi.org/10.1016/j.ejpb.2023.08.016.

References

[1] M.I. Asher, L. García-Marcos, N.E. Pearce, D.P. Strachan, Trends in worldwide asthma prevalence, Eur. Respir. J. 56 (2020) 2002094, https://doi.org/10.1183/13993003.02094-2020.

[2] E.S. Ford, J.B. Croft, D.M. Mannino, A.G. Wheaton, X. Zhang, W.H. Giles, COPD Surveillance-United States, 1999–2011, Chest 144 (2013) 284–305, https://doi.org/10.1378/chest.13-0809.

[3] D. Lu, S.L. Lee, R.A. Lionberger, S. Choi, W. Adams, H.N. Caramenico, B. A. Chowdhury, D.P. Conner, R. Katial, S. Limb, J.R. Peters, L. Yu, S. Seymour, B. V. Li, International Guidelines for Bioequivalence of Locally Acting Orally Inhaled Drug Products: Similarities and Differences, AAPS J. 17 (2015) 546–557, https://doi.org/10.1208/s12248-015-9733-9.

[4] B. Saluja, B.V. Li, S.L. Lee, Bioequivalence for Orally Inhaled and Nasal Drug Products, AAPS Advances in Pharmaceutical Sciences Series, Springer, New York, New York, NY, 2014, pp. 369–394, https://doi.org/10.1007/978-1-4939-1252-0_14.

[5] B. Davit, A.C. Braddy, D.P. Conner, L.X. Yu, International guidelines for bioequivalence of systemically available orally administered generic drug products: A survey of similarities and differences, The AAPS Journal 15 (2013) 974–990, https://doi.org/10.1208/s12248-013-9499-x.

[6] D.R. Kryscio, P.M. Sathe, R. Lionberger, L. Yu, M.A. Bell, M. Jay, J.Z. Hilt, Spreadability Measurements to Assess Structural Equivalence (Q3) of Topical Formulations—A Technical Note, AAPS PharmSciTech 9 (2008) 84–86, https://doi.org/10.1208/s12249-007-9009-5.

[7] V.P. Shah, Progress in methodologies for evaluating bioequivalence of topical formulations, Am. J. Clin. Dermatol. 2 (2001) 275–280, https://doi.org/10.2165/00128071-200102050-00001.

[8] G. Hochhaus, S. Horhota, L. Hendeles, S. Suarez, J. Rebello, Pharmacokinetics of orally inhaled drug products, The AAPS Journal 17 (2015) 769–775, https://doi.org/10.1208/s12248-015-9736-6.

[9] C. Evans, D. Cipolla, T. Chesworth, E. Agurell, R. Ahrens, D. Conner, S. Dissanayake, M. Dolovich, W. Doub, A. Fuglsang, A. García Arieta, M. Golden, R. Hermann, G. Hochhaus, S. Holmes, P. Lafferty, S. Lyapustina, P. Nair, D. O'Connor, D. Parkins, I. Peterson, C. Reisner, D. Sandell, G. J. P. Singh, M. Weda, P. Watson, Equivalence Considerations for Orally Inhaled Products for Local Action—ISAM/IPAC-RS European Workshop Report, Journal of Aerosol Medicine and Pulmonary Drug Delivery 25 (2012) 117–139. doi:10.1089/jamp.2011.0968, pMID: 22413806.

[10] D. O'Connor, W. P. Adams, M.-L. Chen, P. Daley-Yates, J. Davis, H. Derendorf, M. P. Ducharme, A. Fuglsang, M. Herrle, G. Hochhaus, S. M. Holmes, S. L. Lee, B. V. Li, S. Lyapustina, S. Newman, M. Oliver, B. Patterson, J. Peart, G. Poochikian, P. Roy, T. Shah, G. J. P. Singh, S. S. Sharp, Role of pharmacokinetics in establishing bioequivalence for orally inhaled drug products: Workshop summary report, Journal of Aerosol Medicine and Pulmonary Drug Delivery 24 (2011) 119–135. doi:10.1089/jamp.2011.0878, pMID: 21453049.

[11] B. Newman, A. Babiskin, E. Bielski, S. Boc, S. Dhapare, L. Fang, K. Feibus, A. Kaviratna, B.V. Li, M.C. Luke, T. Ma, M. Spagnola, R.L. Walenga, Z. Wang, L. Zhao, N. El-Gendy, C.M. Bertha, M. Abd El-Shafy, D.K. Gaglani, Scientific and regulatory activities initiated by the U.S. Food and Drug Administration to foster approvals of generic dry powder inhalers: Bioequivalence perspective, Advanced Drug Delivery Reviews 190 (2022) 114526, https://doi.org/10.1016/j.addr.2022.114526.

[12] R. Price, G. Farias, W. Ganley, J. Shur, Demonstrating Q3 Structural Equivalence of Dry Powder Inhaler Blends: New Analytical Concepts and Techniques, in: P. R. Bryon, M. Hindle, J. Peart, D. Traini, P.M. Young, S.J. Farr, J.D. Suman, A. Watts (Eds.), Respiratory Drug Delivery 2018, volume 1, 2018, pp. 265–276. River Grove, IL.

[13] R. Price, G. Farias, W. Ganley, J. Shur, Challenging the Bioequivalence Hurdles for OINDPs: Achieving Q3 Structural Equivalence, in: P.R. Bryon, M. Hindle, J. Peart, D. Traini, P.M. Young, S.J. Farr, J.D. Suman, A. Watts (Eds.), Respiratory Drug Delivery Asia 2018, volume 1, 2018, pp. 1–14. River Grove, IL.

[14] P.J. Withers, C. Bouman, S. Carmignato, V. Cnudde, D. Grimaldi, C.K. Hagen, E. Maire, M. Manley, A.D. Plessis, S.R. Stock, X-ray computed tomography, Nature Reviews Methods Primers 1 (2021) 18, https://doi.org/10.1038/s43586-021-00015-4.

[15] T.D. Turner, P. Gajjar, I.S. Fragkopoulos, J. Carr, T.T.H. Nguyen, D. Hooper, F. Clarke, N. Dawson, P.J. Withers, K.J. Roberts, Measuring the Particle Packing of l-Glutamic Acid Crystals through X-ray Computed Tomography for Understanding Powder Flow and Consolidation Behavior, Crystal Growth & Design 20 (2020) 4252–4263, https://doi.org/10.1021/acs.cgd.9b01515.

[16] P. Gajjar, I.D. Styliari, T.T.H. Nguyen, J. Carr, X. Chen, J.A. Elliott, R.B. Hammond, T.L. Burnett, K. Roberts, P.J. Withers, D. Murnane, 3D Characterisation of Dry Powder Inhaler Formulations: Developing X-ray Micro Computed Tomography Approaches, Eur. J. Pharm. Biopharm. 151 (2020) 32–44, https://doi.org/10.1016/j.ejpb.2020.02.013.

[17] F.M. Mahdi, A.P. Shier, I.S. Fragkopoulos, J. Carr, P. Gajjar, F.L. Muller, On the breakage of high aspect ratio crystals in filter beds under continuous percolation, Pharm. Res. 37 (2020), https://doi.org/10.1007/s11095-020-02958-x.

[18] P. Gajjar, T.T.H. Nguyen, J. Sun, I.D. Styliari, H. Bale, S.A. McDonald, T.L. Burnett, B. Tordoff, E. Lauridsen, R.B. Hammond, D. Murnane, P.J. Withers, K.J. Roberts, Crystallographic tomography and molecular modelling of structured organic polycrystalline powders, CrystEngComm 23 (2021) 2520–2531, https://doi.org/10.1039/D0CE01712D.

[19] T.T.H. Nguyen, P. Gajjar, J. Sun, R.B. Hammond, D. Murnane, B. Tordoff, E. Lauridsen, P.J. Withers, K.J. Roberts, Understanding agglomerate intergrowth

crystallisation of hexamine through X-ray microscopy and crystallographic modelling, J. Cryst. Growth (2022) 126986, https://doi.org/10.1016/j.jcrysgro.2022.126986.
[20] W.C. Cosslett, V E and Nixon, Cambridge University Press, X-Ray Microscopy, 1960.
[21] V.E. Cosslett, X-ray Microscopy and Microanalysis, Metallurgical Reviews 5 (1960) 225–266, https://doi.org/10.1179/mtlr.1960.5.1.225.
[22] A.P. Merkle, J. Gelb, The ascent of 3D X-ray microscopy in the laboratory, Microscopy Today 21 (2013) 10–15, https://doi.org/10.1017/S1551929513000060.
[23] L.L. Lavery, J. Gelb, A.P. Merkle, A. Steinbach, X-ray microscopy for hierarchical multi-scale materials, Microscopy Today 22 (2014) 16–21, https://doi.org/10.1017/S155192951400056X.
[24] P. Gajjar, H. Bale, T.L. Burnett, X. Chen, J.A. Elliott, H.V. Gomez, R. Hammond, H. Nguyen, K. Roberts, I.D. Styliari, B. Tordoff, P.J. Withers, D. Murnane, Unlocking the Microstructure of Inhalation Blends using X-Ray Microscopy, in: P. R. Bryon, M. Hindle, J. Peart, D. Traini, P.M. Young, S.J. Farr, J.D. Suman, A. Watts (Eds.), Respiratory Drug Delivery 2020, volume 1, 2020, pp. 101–112. River Grove, IL.
[25] T.L. Burnett, S.A. McDonald, A. Gholinia, R. Geurts, M. Janus, T. Slater, S.J. Haigh, C. Ornek, F. Almuaili, D.L. Engelberg, G.E. Thompson, P.J. Withers, Correlative tomography, Scientific Reports 4 (2014) 4177, https://doi.org/10.1038/srep04711.
[26] T.L. Burnett, P.J. Withers, Completing the picture through correlative characterization, Nat. Mater. 18 (2019) 1041–1049, https://doi.org/10.1038/s41563-019-0402-8.
[27] P. Gajjar, I.D. Styliari, T.L. Burnett, X. Chen, J.A. Elliott, W.J. Ganley, R. Hammond, H. Nguyen, R. Price, K. Roberts, P.J. Withers, D. Murnane, Multiscale Tomography: Probing the Nano-, Micro-, and Meso-scale Resolution of Inhalation Powder Structure, in: P.R. Bryon, M. Hindle, J. Peart, D. Traini, P.M. Young, S. J. Farr, J.D. Suman, A. Watts (Eds.), Respiratory Drug Delivery Europe 2019, volume 1, 2019, pp. 155–168. River Grove, IL.
[28] L.A. Feldkamp, L.C. Davis, J.W. Kress, Practical cone-beam algorithm, Journal of the Optical Society of America A, Optics and Image, Science 1 (1984) 612–619, https://doi.org/10.1364/JOSAA.1.000612.
[29] M. Andrew, L. Omlor, A. Andreyev, S. Ravikumar, M. S. Khoshkhoo, New technologies for X-ray Microscopy: phase correction and fully automated deep learning based tomographic reconstruction, in: B. Müller, G. Wang (Eds.), Developments in X-Ray Tomography XIII, SPIE, 2021, p. 118400I. doi:10.1117/12.2596592.
[30] H. Villarraga-Gómez, A. Andreyev, M. Andrew, H. Bale, R. Sanapala, M. Terada, A. Gu, C. Graf von Hagen, Improving scan time and image quality in 3D X-ray microscopy by deep learning reconstruction techniques 75 (2021) 361–366.
[31] M. Sezgin, B. Sankur, Survey over image thresholding techniques and quantitative performance evaluation, J. Electron. Imaging 13 (2004) 146–165, https://doi.org/10.1117/1.1631315.
[32] T. Hildebrand, P. Rüegsegger, A new method for the model-independent assessment of thickness in three-dimensional images, J. Microsc. 185 (1997) 67–75, https://doi.org/10.1046/j.1365-2818.1997.1340694.x.
[33] F.M. Giorgi, C. Ceraolo, D. Mercatelli, The R Language: An Engine for Bioinformatics and Data Science, Life 12 (2022) 648, https://doi.org/10.3390/life12050648.
[34] A. Videla, C.-L. Lin, J.D. Miller, Watershed Functions Applied to a 3D Image Segmentation Problem for the Analysis of Packed Particle Beds, Particle & Particle Systems Characterization 23 (2006) 237–245, https://doi.org/10.1002/ppsc.200601055.
[35] S. Weis, M. Schröter, Analyzing X-ray tomographies of granular packings, Rev. Sci. Instrum. 88 (2017) 51809, https://doi.org/10.1063/1.4983051.
[36] H. Bale, J. Sun, P. Gajjar, E. Lauridsen, D. Murnane, T.T.H. Nguyen, K.J. Roberts, B. Tordoff, P.J. Withers, Laboratory Diffraction Contrast Tomography (LabDCT): A New Technique for Measuring Crystal Habit and Formulation Structure, in: P. R. Bryon, M. Hindle, J. Peart, D. Traini, P.M. Young, S.J. Farr, J.D. Suman, A. Watts (Eds.), Respiratory Drug Delivery, 3, River Grove, IL, 2020, pp. 765–770.
[37] R. Tuley, J. Shrimpton, M.D. Jones, R. Price, M. Palmer, D. Prime, Experimental observations of dry powder inhaler dose fluidisation, Int. J. Pharm. 358 (2008) 238–247, https://doi.org/10.1016/j.ijpharm.2008.03.038.
[38] J. Shur, H. Harris, M.D. Jones, J.S. Kaerger, R. Price, The Role of Fines in the Modification of the Fluidization and Dispersion Mechanism Within Dry Powder Inhaler Formulations, Pharm. Res. 25 (2008) 1631–1640, https://doi.org/10.1007/s11095-008-9538-y.
[39] G.A. Hebbink, M. Jaspers, H.J.W. Peters, B.H.J. Dickhoff, Recent developments in lactose blend formulations for carrier-based dry powder inhalation, Adv. Drug Deliv. Rev. 189 (2022) 114527, https://doi.org/10.1016/j.addr.2022.114527.
[40] K. Patel, D. Murnane, C. Richardson, F. Liu, A Translation of Technology: MicroCoat™ to Sustained Release Orally Disintegrating Tablets, in: 2022 APS Special Issue 7, 2022, https://doi.org/10.5920/bjpharm.1142.
[41] J.A. Hersey, Ordered mixing: A new concept in powder mixing practice, Powder Technol. 11 (1975) 41–44, https://doi.org/10.1016/0032-5910(75)80021-0.
[42] V. Ramachandran, D. Murnane, R.B. Hammond, J. Pickering, K.J. Roberts, M. Soufian, B. Forbes, S. Jaffari, G.P. Martin, E. Collins, K. Pencheva, Formulation pre-screening of inhalation powders using computational atom-atom systematic search method, Mol. Pharm. (2015), https://doi.org/10.1021/mp500335w.
[43] H. Adi, I. Larson, H. Chiou, P. Young, D. Traini, P. Stewart, Role of agglomeration in the dispersion of salmeterol xinafoate from mixtures for inhalation with differing drug to fine lactose ratios, J. Pharm. Sci. 97 (2008) 3140–3152, https://doi.org/10.1002/jps.21228.
[44] P. Begat, D.A.V. Morton, J.N. Staniforth, R. Price, The Cohesive-Adhesive Balances in Dry Powder Inhaler Formulations II: Influence on Fine Particle Delivery Characteristics, Pharm. Res. 21 (2004) 1826–1833, https://doi.org/10.1023/b:pham.0000045236.60029.cb.
[45] P. Lucas, K. Anderson, J.N. Staniforth, Protein Deposition from Dry Powder Inhalers: Fine Particle Multiplets as Performance Modifiers, Pharm. Res. 15 (1998) 562–569, https://doi.org/10.1023/a:1011977826711.
[46] J. Rudén, G. Frenning, T. Bramer, K. Thalberg, G. Alderborn, Relationships between surface coverage ratio and powder mechanics of binary adhesive mixtures for dry powder inhalers, Int. J. Pharm. 541 (2018) 143–156, https://doi.org/10.1016/j.ijpharm.2018.02.017.